Earth and Planetary Science Letters 297 (2010) 154–164

Contents lists available at ScienceDirect

Earth and Planetary Science Letters

journal homepage: www.elsevier.com/locate/epsl

Constraints on viscous dissipation of plate bending from compressible mantle convection

Wei Leng *, Shijie Zhong

Department of Physics, University of Colorado at Boulder, Boulder, CO 80309, USA

A R T I C L E   I N F O

Article history:
Received 14 January 2010
Received in revised form 8 May 2010
Accepted 8 June 2010
Available online 2 July 2010

Editor: Y. Ricard

Keywords:
plate bending
viscous dissipation
compressible
mantle convection

A B S T R A C T

Tectonic plates on the Earth's surface bend at plate boundaries as they subduct into the mantle, thus generating viscous dissipation. It has been proposed that viscous dissipation due to plate bending accounts for more than 40% of the total viscous dissipation in mantle convection. The proposed large bending dissipation at subduction zones may have significant effects on the Earth's thermal evolution history. However, recent studies show that viscous dissipation from plate bending may not be as significant as previously suggested. Here based on an energetics argument of mantle convection and previously estimated bending dissipation for present-day Earth's subduction zones, we show that the total dissipation in the Earth's mantle is 10.0–15.5 TW and that the bending dissipation only accounts for <10% of the total dissipation in the Earth's mantle convection. We also determine the ratio of the bending dissipation to the total viscous dissipation using compressible mantle convection models within a large parameter space. The bending dissipation accounts for 10% to 20% of the total dissipation for cases with only temperature-dependent viscosity. For cases with a weak upper mantle, the bending dissipation accounts for less than 10% of the total dissipation. These results from numerical models further support the conclusion that the bending dissipation only accounts for a small fraction (<10%) of the total viscous dissipation. Our results suggest that in studying plate motions and long-term thermal evolution of the Earth, other convective processes in the mantle play probably more important roles than plate bending.

1. Introduction

It is generally agreed that surface plate tectonics on the Earth is mainly driven by the negative buoyancy of subducted slabs. As a plate subducts beneath an overriding plate, the plate bending causes significant viscous dissipation, thus representing an important resisting force to plate motion (McKenzie, 1977; Conrad and Hager, 1999a). It has been proposed that the viscous dissipation and resisting force to plate motion associated with plate bending may have significant effects on convective heat transfer and thermal evolution history of the Earth's mantle (Conrad and Hager, 1999b). Particularly, considering the plate bending as the only major resisting force to convective motion and potential effects of melting on mantle lithospheric viscosity in a parameterized mantle convection model, Korenaga (2006) suggested that convective heat flux may decrease with increasing convective vigor or Rayleigh number *Ra*. Korenaga's model provides a non-intuitive relationship between heat flux and *Ra* and may help avoid excessively high temperature for the early Earth that are predicted by other parameterized convection models with low radiogenic heating rate (e.g., Davies, 1993; 2009). However, the amount of viscous dissipation generated at subduction zones has been a matter of great debate recently (Conrad and Hager, 1999a, 2001; Buffett and Rowley, 2006; Capitanio et al., 2007, 2009; Krien and Fleitout, 2008; Wu et al, 2008; Schellart, 2009; Davies, 2009).

By applying fixed subduction geometry, Conrad and Hager (1999a, 2001) well simulated the bending effects of the subducted plates in 2-D Cartesian geometry with numerical models, and concluded that viscous dissipation due to bending is mainly controlled by the radius of curvature of subducted slabs, R_c, and the effective viscosity of the lithosphere, η_l. The bending dissipation is proportional to η_l and the inverse cube of R_c, and is therefore very sensitive to the variations of R_c. Assuming $R_c = 200$ km, Conrad and Hager (2001) suggested that the bending dissipation can be up to 40% of the mantle's total dissipation, and for a thick plate this percentage may be even larger (Conrad and Hager, 1999a). Considering realistic plate geometry and plate motions but also assuming a radius of curvature of subducted slabs $R_c = 200$ km, Buffett (2006) estimated the plate bending force for major plates, and concluded ~40% of the gravitational energy of subducted slabs in the upper mantle is dissipated by bending dissipation for the Pacific plate (Buffett and Rowley, 2006). For all the major plates, the ratio is smaller, ~25% (Buffett and Rowley, 2006). Although Buffett and Rowley (2006) considered whole mantle convection, they did not discuss how much the bending dissipation

* Corresponding author.
E-mail address: wei.leng@colorado.edu (W. Leng).

0012-821X/$ – see front matter
doi:10.1016/j.epsl.2010.06.016

would account for the total dissipation for the whole mantle. In the thermal evolution calculations by Korenaga (2006), R_c is also assumed to be 200 km.

Recently, observational studies, and numerical and laboratory modeling all show that viscous dissipation from plate bending may be significantly smaller than previously suggested (Wu et al., 2008; Capitanio et al., 2007, 2009; Krien and Fleitout, 2008; Schellart, 2009). Wu et al. (2008) compiled the radius of curvature R_c globally in 207 subduction zones from slab seismicity and estimated the average R_c as 390 km, which is nearly twice of the previous estimate of 200 km (Conrad and Hager, 1999a, 2001), implying a reduction of bending dissipation by a factor of 8. Capitanio et al. (2007, 2009) studied the dynamics and energetics of a free subduction system and found that bending curvature and dip angle dynamically adjust to minimize the plate bending dissipation. They argued that the bending dissipation is independent of the lithosphere viscosity η_l due to this self-regulating mechanism, and that the ratio of bending dissipation to total dissipation in the Earth's mantle is less than 20%. Krien and Fleitout (2008) proposed that in order to reproduce the short- to intermediate-wavelength gravity and geoid anomalies observed in subduction zones, more than 70% of the total dissipation should be generated in the sublithospheric mantle, and only 10%–20% dissipation is generated in the bending zones. With 3-D laboratory studies on subduction, Schellart (2009) suggested that the bending dissipation is 6% to 22% of the total dissipation, and that it increases with increased viscosity contrast between the lithosphere and the upper mantle. This dependence of the bending dissipation on the lithospheric viscosity is different from Capitanio et al. (2007, 2009) who suggested that the bending dissipation is independent of the lithosphere viscosity but is consistent with suggestions by Conrad and Hager (1999a, 2001). Based on these studies, Davies (2009) questioned the results of large bending dissipation in subduction zones and the validity of thermal evolution models suggested by Korenaga (2006).

In the above-mentioned modeling studies of bending dissipation in subduction zones, the slabs are either modeled with Stokes flow model or convection model with Boussinesq approximation (Conrad and Hager, 1999a, 2001; Buffett and Rowley, 2006; Capitanio et al., 2007, 2009). The total viscous dissipation in these models can be determined accurately, provided that the mantle buoyancy flux structure is known precisely (e.g. Conrad and Hager, 1999a). However, the buoyancy flux structure in the Earth's mantle is not well constrained, particularly for the slab buoyancy in the lower mantle and the plume buoyancy. Most of the previous studies only considered the slab buoyancy flux in the upper mantle as the total buoyancy flux (Conrad and Hager, 1999a, 2001; Capitanio et al., 2007, 2009), and may underestimate the total dissipation in the Earth's mantle. Hewitt et al. (1975) suggested an independent method to estimate the total dissipation based on a more complete compressible mantle convection formulation. In Hewitt et al.'s (1975) method, the total mantle dissipation can be directly estimated from convective surface heat flux, internal heating ratio, and mantle thermodynamic parameters, with no need for detailed knowledge of mantle convective structure. In addition, the compressible mantle convection model that includes viscous heating and adiabatic heating as energetic components may significantly influence the convection and dissipation patterns (Bercovici et al., 1992; Balachandar et al., 1995, Leng and Zhong, 2008b).

Here, we formulate a compressible whole mantle convection model to study viscous dissipation for the whole convection system and also for subduction zones. We first provide a new and robust constraint on total dissipation of the Earth's mantle convection, using observed convective surface heat flux and thermodynamic properties of the Earth's mantle (Hewitt et al., 1975). We then quantify the bending dissipation in our numerical models for cases within a large parameter space. After discussing the implications of our results, we draw our main conclusions.

2. Constraints on total viscous dissipation from the energetics

Based on an energy balance argument, Hewitt et al. (1975) has demonstrated that the total dissipation in a compressible thermal convection system is given by

$$\Phi_{tot} \approx D_i(1-0.5\mu)Q_s, \tag{1}$$

where Φ_{tot}, μ and Q_s are the total dissipation, internal heating ratio of the mantle, and surface heat flux, respectively. D_i is the dissipation number which is defined as

$$D_i = \alpha_0 g_0 d / C_{p\_0}, \tag{2}$$

where α_0, g_0 and C_{p_0} are the reference thermal expansivity, gravitational acceleration and specific heat (e.g. at the Earth's surface), respectively; and d is the mantle thickness. Eq. (1) can be analytically derived for compressible thermal convection independent of mantle rheology (Hewitt et al., 1975), and it has been proven valid in numerical models for isoviscous thermal convection when the Rayleigh number, Ra, of the convection system is much larger than a critical Rayleigh number (Hewitt et al., 1975; Jarvis and McKenzie, 1980). This relation has been employed to estimate the maximum stresses on plate boundaries (McKenzie and Jarvis, 1980).

Eq. (1) was derived for a Cartesian geometry (Hewitt et al., 1975). Recently, Leng and Zhong (2009) showed that for the Earth's mantle in a spherical geometry, Eq. (1) becomes

$$\Phi_{tot} \approx D_i(1-0.594\mu)Q_s. \tag{3}$$

Eq. (3) has been used to put constraints on mantle internal heating ratio based on plume heat flux (Leng and Zhong, 2009).

The total surface heat flux of the Earth is ~44 TW with ~8 TW from the radiogenic heating in the continental crust (e.g., Pollack et al., 1993; Davies, 1999). The remaining ~36 TW is from the mantle and can be considered as convective heat flux, or Q_s. The dissipation number of the mantle, D_i, is estimated to be 0.5–0.7. Observations of mantle plume excess temperature and buoyancy flux constrain that the internal heating ratio of the mantle is ~70% (Zhong, 2006; Leng and Zhong, 2008b). If we consider the internal heating ratio of the mantle varying between 65% and 75%, Eq. (3) provides a possible range for the total dissipation in the Earth's mantle between 10.0 TW and 15.5 TW, as shown in Fig. 1. Buffett and Rowley (2006) estimated the bending dissipation for all the major subduction zones as ~0.766 TW, which is likely an upper bound given that their calculations assumed a radius of curvature $R_c = 200$ km and relatively large lithospheric viscosity of 6×10^{22} Pa s at the subduction bending zones. This upper bound of the bending dissipation suggests that the bending dissipation at subduction zones for the present-day Earth at most accounts for only 5%–8% of the total dissipation, which is significantly smaller than ~40% as suggested in previous studies (Conrad and Hager, 1999a, 2001). The total dissipation is larger for smaller internal heating ratio (Fig. 1) which may be favored by geochemistry-based thermal models (e.g. Korenaga, 2006).

3. Results from compressible mantle convection models

3.1. Numerical modeling and quantifying model results

We then directly quantify the bending dissipation with numerical models. We use a 2-D Cartesian finite element mantle convection code which is modified from Citcom (Moresi et al., 1996) to include the mantle compressibility with anelastic liquid approximation (ALA) (Leng and Zhong, 2008a; King et al., 2010). The governing

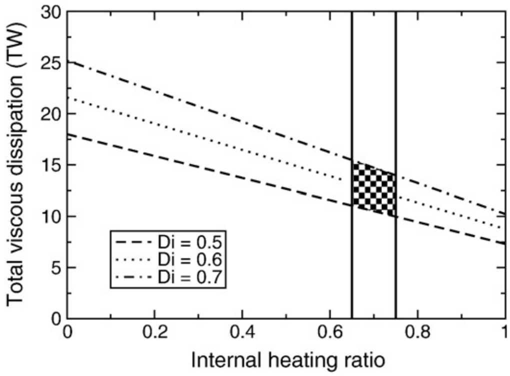

Fig. 1. The possible range of total viscous dissipation in the Earth's mantle (dotted region). This range is derived from Eq. (3) with the dissipation number varying between 0.5 and 0.7 and the internal heating ratio of the mantle varying between 65% and 75%.

conservation equations of mass, momentum and energy in non-dimensional form are as following:

$$(\rho_r u_i)_{,i} = 0, \tag{4}$$

$$-p_{,j}\delta_{ij} + \tau_{ij,j} + \left[\rho_r \alpha g Ra (T - T_r) - \frac{\alpha g}{C_p \Gamma} p \chi\right]\delta_{i3} = 0, \tag{5}$$

$$\rho_r C_p \dot{T} + \rho_r C_p u_i T_{,i} + \rho_r \alpha g D_i u_3 (T + T_s) = \left(k T_{,i}\right)_{,i} + \frac{D_i}{Ra}\tau_{ij} u_{i,j} + \rho_r H, \tag{6}$$

where ρ_r, u, p, τ, α, g, T, T_r, C_p, Γ, T_s, k and H are radial density, velocity vector, dynamic pressure, deviatoric stress tensor, thermal expansivity, gravitational acceleration, temperature, reference temperature, specific heat at constant pressure, Grueneisen parameter, surface temperature, thermal conductivity and heat production rate, respectively; i and j are spatial indices and 3 means vertical direction; δ is the Kronecker delta function. $\dot{T}$ is the derivative of temperature with respect to time t. The Rayleigh number Ra and mantle compressibility χ are defined as

$$Ra = \frac{\rho_0 \alpha_0 g_0 \Delta T d^3}{\kappa_0 \eta_0}, \tag{7}$$

$$\chi = \frac{D_i}{\Gamma_0}, \tag{8}$$

where ρ_0, ΔT, κ_0, η_0 and Γ_0 are the surface density, temperature difference between the surface and the core–mantle boundary, surface thermal diffusivity, reference viscosity and surface Grueneisen parameter, respectively. Details of the derivation of these equations can be found in Leng and Zhong (2008a). Notice that we use mantle thickness $d = 2870$ km and temperature difference between the surface and the core–mantle boundary $\Delta T = 3000$ K to nondimensionalize the length and temperature in this study.

For simplicity, we assume α, g, C_p, Γ, and k are all constants in the mantle. As a result, these parameters become 1.0 in non-dimensional Eqs. (4)–(6). Γ_0 is set to be 1.0 in our models, so mantle compressibility χ is the same as dissipation number D_i from Eq. (8). We employ Adams–Williamson equation (Birch, 1952) as the equation of state, so the radial density profile ρ_r is given as (Leng and Zhong, 2008a)

$$\rho_r(z) = \exp[(1 - z)\chi], \tag{9}$$

where z is the non-dimensional vertical distance.

We use 257 by 129 grids in a two by one box with mesh refinements in the top and bottom thermal boundary layers (TBL). The boundaries are free-slip, and isothermal for top and bottom boundaries and insulated for sidewalls. For most of our models, we do not include internal heating generation, but we also test the effect of internal heating on our results later. The non-dimensional temperature is fixed as 0.0 and 1.0 at the top and bottom boundaries, respectively.

We employ a depth- and temperature-dependent rheology as

$$\eta(T, z) = \eta_r(z)\exp[-A(T - T_{adi}(z))], \tag{10}$$

where η, T, A and $T_{adi}(z)$ are the viscosity, temperature, activation energy and adiabatic temperature at z, respectively. $\eta_r(z)$ is the depth-

Table 1
Model parameters and results.[a]

Cases	Ra	D_i	V_c	Q_s	U_{rms}	U_s	U_{um}/U_s	ε(%)	Φ_{tot}/Q_s	Φ_b/Φ_{tot}
A01	10^7	0.5	10^5	7.46	544.4	251.1	1.3	2.4	0.422	0.181
A02	10^7	0.5	10^0	23.28	1298.3	1190.1	1.0	−0.6	0.485	0.059
A03	10^7	0.5	10^1	20.80	1273.5	1064.7	1.1	−0.4	0.482	0.098
A04	10^7	0.5	10^2	17.66	1138.3	763.1	1.2	−0.5	0.488	0.134
A05	10^7	0.5	10^3	13.16	913.8	512.7	1.3	0.2	0.462	0.166
A06	10^7	0.5	10^4	10.14	753.9	338.1	1.4	−0.5	0.448	0.166
A07	10^7	0.5	10^6	4.55	440.8	65.6	1.3	−0.3	0.374	0.111
A08	10^8	0.5	10^6	10.10	1685.1	464.0	1.6	4.2	0.447	0.134
B01	10^6	0.3	10^5	3.07	118.9	14.5	1.1	0.4	0.199	0.098
B02	5×10^6	0.3	10^5	4.72	337.7	47.7	1.3	1.5	0.236	0.112
B03	10^7	0.3	10^5	5.74	530.7	69.2	1.5	1.7	0.243	0.106
B04	5×10^7	0.3	10^5	10.81	1583.6	367.1	1.6	4.4	0.270	0.155
B05	10^8	0.3	10^5	13.64	2398.4	603.6	1.7	5.3	0.273	0.154
B11	10^6	0.5	10^5	3.70	142.0	46.4	1.1	1.5	0.350	0.172
B12	5×10^6	0.5	10^5	5.36	338.1	101.6	1.2	0.3	0.392	0.152
B13	5×10^7	0.5	10^5	11.93	1564.6	662.4	1.2	1.3	0.449	0.161
B14	10^8	0.5	10^5	13.12	2014.6	284.1	3.0	−0.6	0.465	0.132
B21	10^6	0.7	10^5	3.43	136.7	23.1	1.5	−1.5	0.471	0.112
B22	5×10^6	0.7	10^5	5.60	284.6	103.2	1.4	−2.5	0.560	0.156
B23	10^7	0.7	10^5	6.54	514.5	173.4	1.4	−1.6	0.575	0.149
B24	5×10^7	0.7	10^5	11.78	1210.7	735.3	1.3	0.8	0.661	0.150
B25	10^8	0.7	10^5	14.89	2097.8	1110.3	1.4	1.6	0.678	0.158

[a] Ra, D_i, V_c, Q_s, U_{rms}, U_s, U_{um}, ε, Φ_{tot} and Φ_b are the Rayleigh number, dissipation number, viscosity contrast, surface heat flux, rms velocity, surface velocity, upper mantle velocity, relative difference between the total viscous dissipation and the total adiabatic heating, total viscous dissipation and the viscous dissipation in the bending zones, respectively. ε is computed as $\varepsilon = (E_v - E_a)/E_v$, where E_v and E_a are the total viscous dissipation and the total adiabatic heating. All these values are non-dimensional.

dependent viscosity parameter. We use $\eta_r(z) = 1.0$ throughout the whole mantle for most cases unless stated otherwise. However, we also test the effect of a weak upper mantle on our results by reducing $\eta_r(z)$ in the upper mantle. In order to compute $T_{adi}(z)$, we take the horizontally averaged temperature at the middle depth of the mantle as the reference temperature, $T_{adi}(z)$ is then computed by integrating adiabatic temperature gradient to different depth (Turcotte and Schubert, 2002, page 187). The activation energy A controls the temperature-induced viscosity variations. We use $V_c = \exp(A)$ to describe the total viscosity contrast for different cases hereafter, although the actual total viscosity contrast is slightly smaller because of the removal of the adiabatic temperature in Eq. (10).

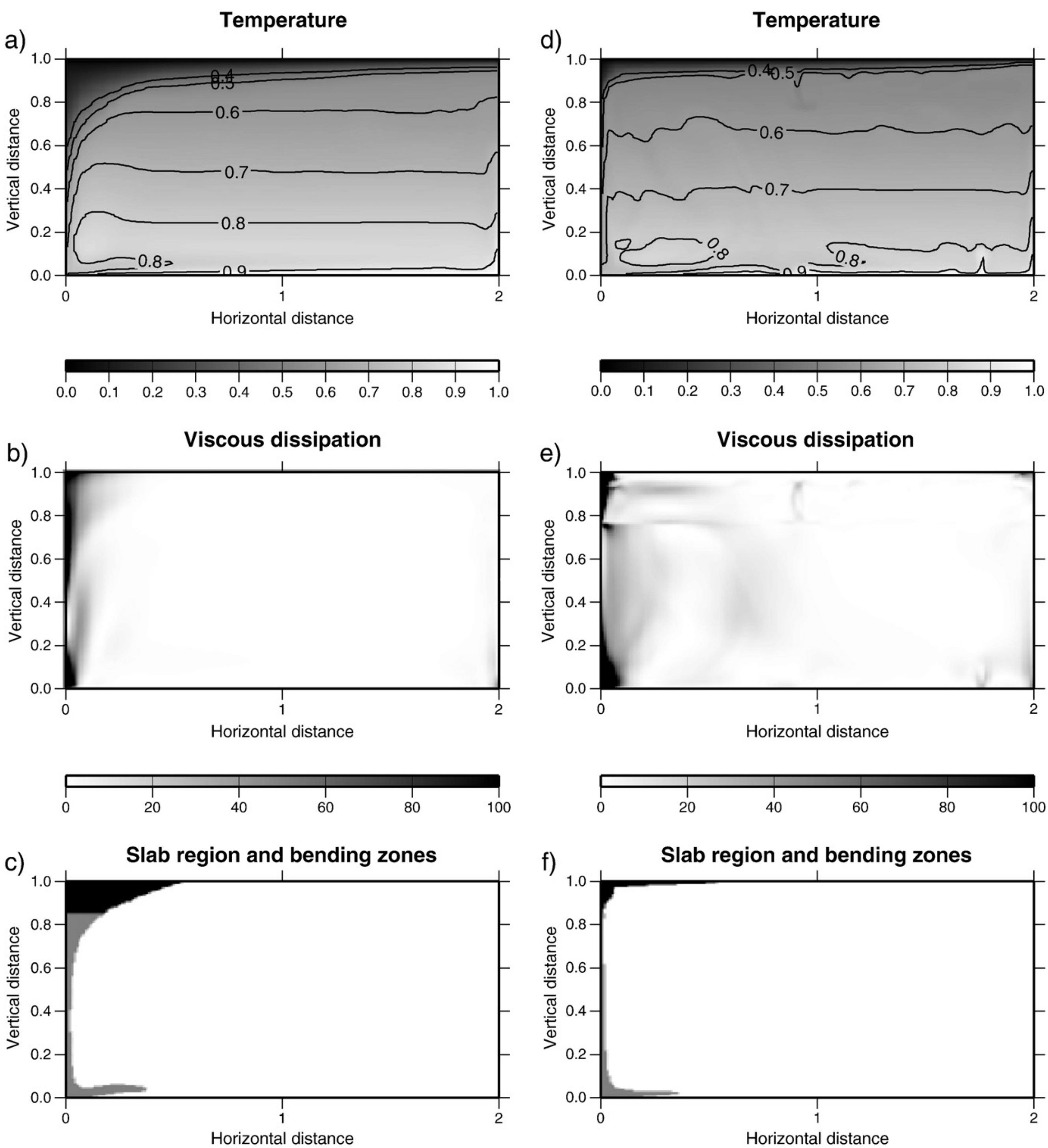

Fig. 2. (a) A snapshot of the temperature field after case A01 reaches a statistically steady state. (b) The distribution of viscous dissipation for temperature field shown in Fig. 2a. (c) The grey area shows the identified slab region and the black area shows the identified bending zones for temperature field shown in Fig. 2a. Notice that the bending zones are included in the slab area. (d), (e) and (f) are similar to (a), (b) and (c), except that they represent a snapshot for case D03 after it reaches a statistically steady state. All these values are non-dimensional.

In this study, we run each case for 100,000–200,000 time steps to a statistically steady state and analyze the steady state results for the final 20,000 time steps to obtain time-averaged values. It has been theoretically and numerically demonstrated that in a compressible mantle convection system the total adiabatic heating and total viscous heating (i.e. viscous dissipation) should exactly balance out each other at any instant in time (Leng and Zhong, 2008a). We use this principle to test the energy consistency of the results of our models. In all of our models, we typically observe ~1% or less imbalance between the total adiabatic heating and total viscous heating. Although for some cases with high Rayleigh numbers and complicated rheology this imbalance can be up to 3–5% (details will be presented in the results section). We thus consider that the energy consistency is satisfied in our models.

Before we can quantify viscous dissipation in the bending zones, we first need to define the bending zones in our numerical models. We use temperature criteria to define the slab region. A region is defined as slab region if its temperature T satisfies,

$$T<T_{ave}(z)+f_t[T_{\min}(z)-T_{ave}(z)], \tag{11}$$

where $T_{ave}(z)$ and $T_{\min}(z)$ are averaged temperature and minimum temperature at vertical distance z, and f_t is a prescribed threshold constant. The bending zones are also defined with temperature criteria shown by Eq. (11), but are confined to a shallow depth controlled by a non-dimensional bending zone depth f_d. We will discuss the effects of parameters f_t and f_d on the detection of the slab region and bending zones later.

3.2. Plate bending dissipation for different lithospheric viscosities

We first present results for a case A01 with $Ra=10^7$, $D_i=0.5$, $V_c=10^5$ and no internal heating. The non-dimensional time-averaged surface heat flux, Q_s, root-mean-square (rms) velocity, U_{rms}, and surface velocity, U_s, are determined as 7.46, 544.4, and 251.1, respectively, after the case reaches a statistically steady state (Table 1). Fig. 2a shows a typical snapshot of the temperature field for case A01. The horizontally averaged temperature follows the adiabatic temperature profiles quite well (Fig. 3a). The horizontally averaged viscosity is ~1.0 in the interior of the mantle and gradually increases to several hundred at the surface (Fig. 3a). For each case in this study, we also report the relative difference, ε, between the total viscous dissipation, E_v, and the total adiabatic heating, E_a. ε is defined as $\varepsilon=(E_v-E_a)/E_v$. A smaller ε reflects better energy consistency as we discussed above. For case A01, ε is 2.4% (Table 1). We define the average velocity at ~300 km depth as the upper mantle velocity, U_{um}. The ratio of the upper mantle velocity to the surface velocity reflects the relative motion between the surface and the upper mantle. For case A01, U_{um}/U_s is 1.2 (Table 1).

In order to define the slab region and bending zones, we set parameters $f_t=0.5$ and $f_d=0.139$, the latter implying that the bending zones only extend to 400 km depth, given that the depth of the mantle is 2870 km. Viscous dissipation and the detected slab region and bending zones are shown in Fig. 2b and c. It can be observed that although the dissipation is large in the bending zone, strong dissipation also happens in subducted slabs at large depths of the mantle (Fig. 2b). This can also be seen in Fig. 3b which shows the horizontally averaged viscous dissipation. Although the dissipation is maximum near the top surface where the slabs bend, significant dissipation happens almost uniformly along the depth. We quantify the dissipation in the bending zone, Φ_b, and the total dissipation in the system, Φ_{tot}. The ratio of Φ_b/Φ_{tot} fluctuates with time for case A01 after it reaches a statistically steady state (Fig. 4), and the time-averaged value is 18% (Table 1).

We examined the effects of detection parameters f_t and f_d on our results. Varying f_t from 0.5 to 0.3 or 0.7 leads to a ~1.0% difference and varying f_d such that the maximum depth for bending zones change from 400 km to 300 km or 500 km leads to a ~3.0% difference for our results of Φ_b/Φ_{tot} (Fig. 4). We thus keep using $f_t=0.5$ and $f_d=0.139$ (i.e., 400 km depth) hereafter in this study. It is worthwhile to point out that our detection parameters tend to yield larger bending zones hence an upper bound of bending dissipation.

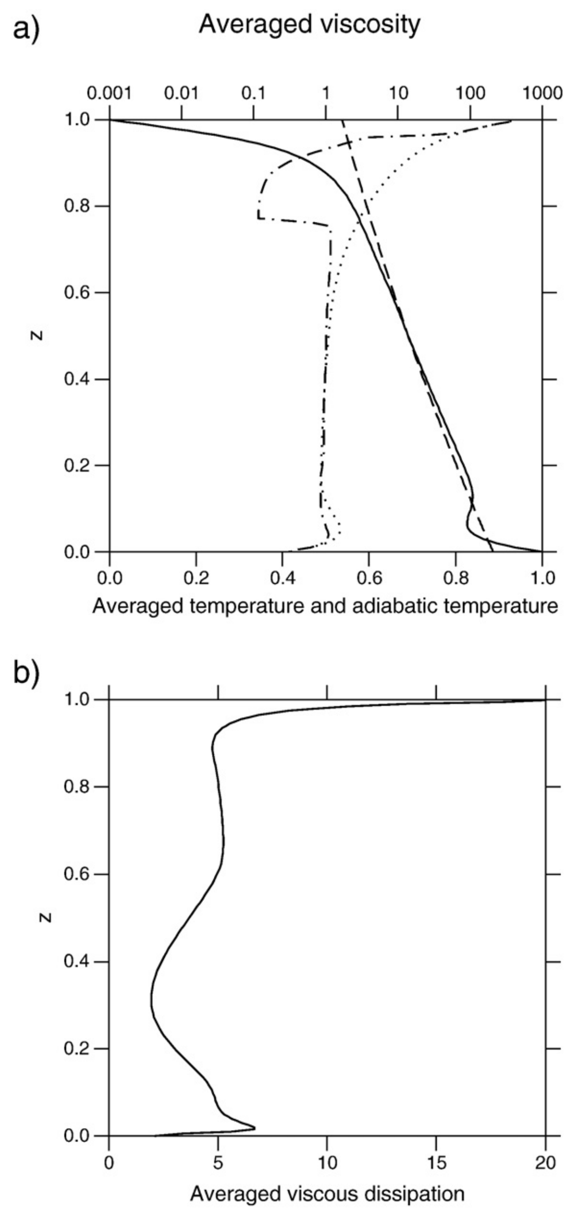

Fig. 3. (a) Horizontally averaged temperature (solid line) and viscosity (dotted line) and computed adiabatic temperature (dashed line) for the temperature field shown in Fig. 2a. The dotted-dashed line shows a snapshot of the horizontally averaged viscosity for case C01 with layer viscosity structure. (b) Horizontally averaged viscous dissipation for the temperature field shown in Fig. 2a. All these values are non-dimensional.

We then compute a series of cases A02–A07 that are identical to the case A01, except that the viscosity contrast V_c varies from 1 to 10^6 (Table 1). The results show that Φ_b/Φ_{tot} generally increases with V_c for viscosity contrast between 1 and 10^3 (Fig. 5). However, for large V_c which is more appropriate for the Earth's mantle, Φ_b/Φ_{tot} is no longer sensitive to V_c and varies between 10% and 20% (Fig. 5). With $V_c=10^6$, the top thermal boundary layer becomes very thick and convection approaches a stagnant-lid convection regime due to strong

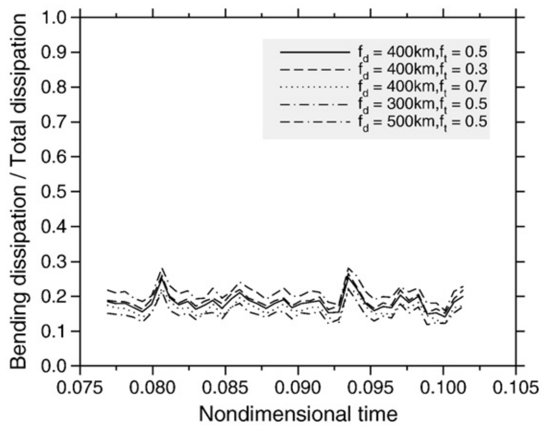

Fig. 4. The ratio of the viscous dissipation in the bending region to the total dissipation versus time for case A01 after it reaches a statistically steady state. Different curves represent results from different bending region detection criteria.

lithospheric viscosity (Moresi and Solomatov, 1995). We quantify the thickness of the top thermal boundary layer for cases A01–A07 with a simple scheme. The horizontally averaged temperature profile for each case is first computed. Then, the thickness of the top thermal boundary layer is defined as the distance between the surface and the depth where the average temperature is equal to 1300 °C. This method

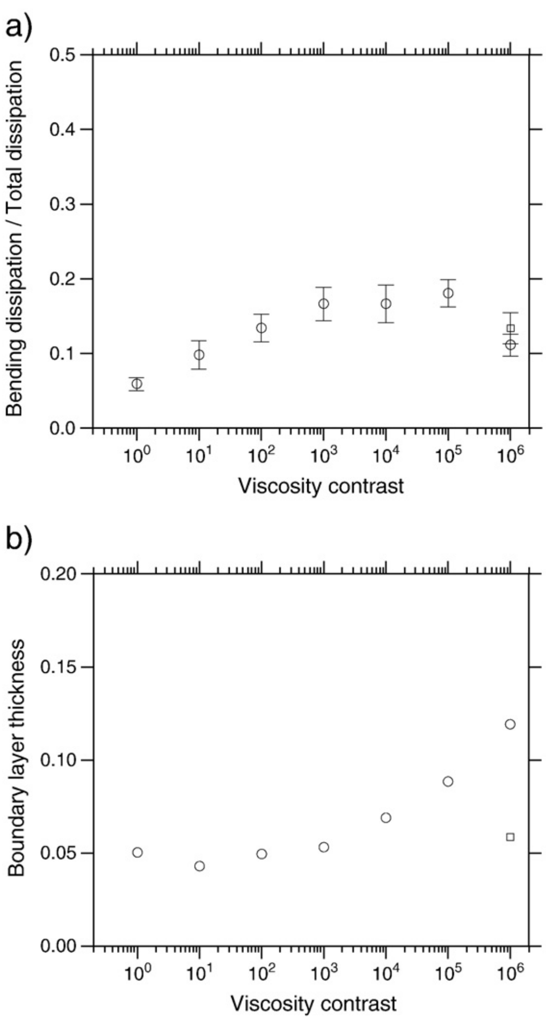

Fig. 5. (a) The ratios of the viscous dissipation in the bending region to the total dissipation for cases with different activation energy (i.e. different viscosity contrast V_c). The circles represent cases with $D_i = 0.5$ and $Ra = 10^7$, (cases A01–A07 in Table 1) and the square represents a case (A08 in Table 1) with $D_i = 0.5$ and $Ra = 10^8$. The error bars show the standard deviations over the analyzed time period. (b) The non-dimensional thickness of the top thermal boundary layer for the cases shown in (a). The circles represent cases A01–A07, and the square represents case A08.

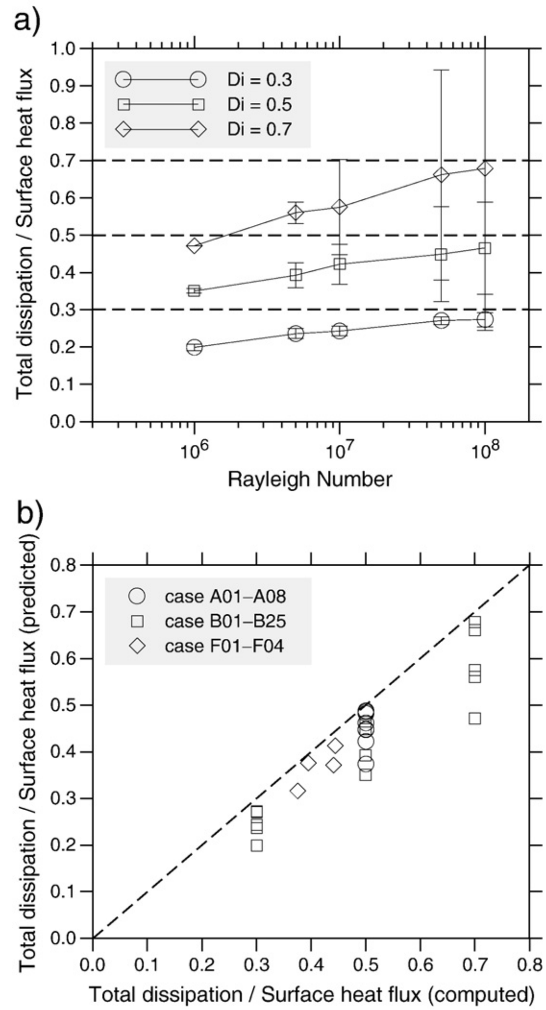

Fig. 6. (a) The ratios of the total dissipation to surface heat flux for cases with different Ra and D_i (cases B01–B25 and case A01 in Table 1). (b) The predicted ratios versus the numerically computed ratios of the total dissipation to surface heat flux (circles: cases A01–A08, squares: cases B01–B25, diamonds: cases F01–F04).

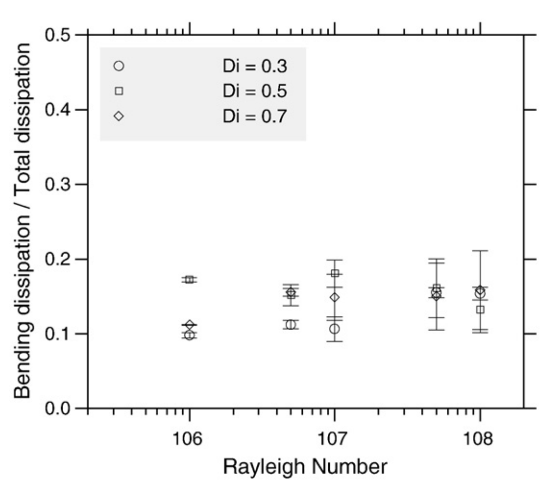

Fig. 7. The ratios of the viscous dissipation in the bending region to the total dissipation for cases with only temperature-dependent viscosity but different Ra and D_i (cases B01–B25 and case A01 in Table 1).

may not be perfectly precise, but is good enough to show the thickness variation of the top thermal boundary layer with increased viscosity contrast (Fig. 5b). For case A07 with $V_c = 10^6$, the top thermal boundary layer becomes extremely thick. We increase the Rayleigh number for the case A07 with $V_c = 10^6$ from $Ra = 10^7$ to $Ra = 10^8$ (i.e. case A08) to reduce the thickness of the top thermal boundary layer (Fig. 5b). Φ_b/Φ_{tot} increases slightly as a result of the increase of Rayleigh number, but still lies between 10% and 20% (Fig. 5).

3.3. Plate bending dissipation for different Rayleigh numbers and dissipation numbers

Hewitt et al. (1975) and Jarvis and McKenzie (1980) confirmed Eq. (1) through comparing the surface heat flux and total viscous dissipation in numerical models with different Rayleigh numbers and dissipation numbers. However, their calculations were only done for isoviscous cases. Here we examine Eq. (1) for cases with strongly temperature-dependent viscosity. We compute a series of cases B01–B25 with the same viscosity contrast $V_c = 10^5$ and no internal heating, but different Ra and D_i (Table 1).

Fig. 6a shows the ratios of total dissipation to surface heat flux for cases B01–B25 and A01. It can be seen that for a given dissipation number, the ratio approaches the dissipation number, even for cases which have large D_i and strong time variability. This is exactly the prediction from Eq. (1) and is very similar to the results shown by Hewitt et al. (1975) and Jarvis and McKenzie (1980) for isoviscous cases. Fig. 6b plots the predicted ratios from Eq. (1) and the numerically computed ratios for all the cases shown in Table 1. Fig. 6a and b show that Eq. (1) provides accurate descriptions of the dependence of the total viscous dissipation on the dissipation number and surface heat flux in compressible mantle convection with variable viscosity, especially for cases with large Rayleigh numbers. For all these cases, the ratios of the bending dissipation to the total dissipation, Φ_b/Φ_{tot}, are all between 10% and 20% and insensitive to the Rayleigh number, mantle viscosity and dissipation number (Fig. 7).

One point we want to point out is that the surface velocity for the case B14 is anomalously small (e.g. compared to the case B13). This is because with increased Rayleigh number, the convection wavelength decreases for this case with more convection cells formed and the surface velocity significantly decreases.

3.4. Plate bending dissipation with layered viscosity, weak zones and internal heat generation

We have so far only considered temperature-dependent viscosity and neglected internal heat generation and depth-dependent viscosity that may be important to the Earth's mantle convection. In this subsection, we add more realistic rheology and internal heat generation to our models to study their effects on the ratio of the bending dissipation to the total dissipation.

First, an upper mantle with smaller viscosity relative to the lower mantle is proposed from the studies of the Earth's long-wavelength geoid (Hager and Richards, 1989). We incorporate the viscosity stratification in our models by reducing $\eta_r(z)$ in the upper mantle (i.e., between 100 km and 660 km depths). Cases C01–C04 are the same as case A01, except that $\eta_r(z)$ in the upper mantle is reduced from 1 to 1/10, 1/20, 1/30 and 1/50, respectively (Table 2). A snapshot of the horizontally averaged viscosity profile for case C01 is shown in Fig. 3a. The ratio of the bending dissipation to the total dissipation, Φ_b/Φ_{tot}, for cases C01–C04 is ~5% (Fig. 8a, Table 2), which is much smaller than that for case A01. This is because the viscosity contrast between the surface and the upper mantle increases significantly due to the reduced upper mantle viscosity, so does the velocity contrast between the surface and the upper mantle (Table 2). The convection therefore approaches a stagnant-lid convection regime with very small surface velocity and plate bending dissipation (Table 2) (Moresi and Solomatov, 1995). Another reason for the reduction of the bending dissipation is that the convective velocity in the upper mantle with reduced viscosity is greatly enhanced, thus thinning the downwelling slabs and reducing the area of the bending zones.

To achieve more realistic surface plate behavior, we introduce weak zones into our layered viscosity models to simulate the effects of nonlinear deformation at plate margins (e.g., Gurnis, 1989). Case D01–D05 are the same as the case C03, i.e. also with a weak upper mantle, except that we add two weak zones at the upper-left and upper-right corners (See Fig. 9 for the position of weak zones). The weak zones are 200 km by 200 km in size, and the non-dimensional viscosity in the weak zones is fixed as a constant, η_{weak}, for each case (see Table 2). For case D01, the weak zone viscosity is fixed as 100.0, which does not deviate much from the viscosity structure in case C03. As a result, the surface heat flux, rms velocity and the ratio Φ_b/Φ_{tot} for case D01 are quite similar to those for case C03 (Table 2). Fig. 8b shows the ratio Φ_b/Φ_{tot} and the averaged surface velocity versus the

Table 2
Model parameters and results for cases with more realistic physics.[a]

Cases	η_{um}	η_{weak}	μ(%)	Q_s	U_{rms}	U_s	U_{um}/U_s	ε(%)	Φ_{tot}/Q_s	Φ_b/Φ_{tot}
C01	1/10	–	0	7.19	1136.1	166.1	4.1	−0.8	0.437	0.059
C02	1/20	–	0	7.53	1401.1	149.0	8.3	−3.3	0.441	0.042
C03	1/30	–	0	7.78	1646.1	130.8	13.3	−4.5	0.445	0.039
C04	1/50	–	0	8.16	2214.5	145.7	20.7	1.2	0.477	0.035
D01	1/30	100.0	0	7.75	1632.9	140.5	12.4	−3.4	0.440	0.029
D02	1/30	30.0	0	8.89	1625.5	282.6	6.6	−2.1	0.454	0.056
D03	1/30	10.0	0	11.11	1605.3	598.5	3.5	−4.5	0.461	0.083
D04	1/30	3.0	0	14.46	1564.3	1245.9	1.7	−3.1	0.475	0.104
D05	1/30	1.0	0	17.16	1516.1	1930.8	1.2	−1.1	0.483	0.085
E01	1/30	3.0	0	13.17	1879.5	967.2	2.7	−2.4	0.480	0.086
E02	1/30	1.0	0	14.93	1832.3	1365.1	1.9	−1.9	0.478	0.100
E03	1/30	0.3	0	17.19	1804.4	1891.6	1.3	−2.3	0.483	0.106
E04	1/30	0.1	0	18.53	1704.1	2279.3	1.0	5.0	0.482	0.128
E05	1/30	0.03	0	18.91	1597.7	2493.9	0.8	1.5	0.480	0.121
F01	1	–	19.9	6.70	460.8	185.7	1.2	−1.2	0.371	0.173
F02	1	–	42.0	6.17	378.3	133.3	1.2	−4.2	0.316	0.151
F03	1/30	10.0	18.9	10.91	1386.5	130.5	4.5	−3.4	0.413	0.078
F04	1/30	10.0	35.5	10.96	1291.0	85.4	6.2	−2.9	0.376	0.080

[a] η_{um}, η_{weak} and μ are the $\eta_r(z)$ in the upper mantle, viscosity in the weak zone, and internal heating ratio, respectively. All the values are non-dimensional. μ is computed as $\mu = (Q_s - Q_b)/Q_s$, where Q_s and Q_b are surface heat flux and bottom heat flux. For cases C01–C04, D01–D05 and F01–F04, $Ra = 10^7$, $D_i = 0.5$ and $V_c = 10^5$. For cases E01–E05, $Ra = 10^7$, $D_i = 0.5$, but V_c is reduced to 10^4.

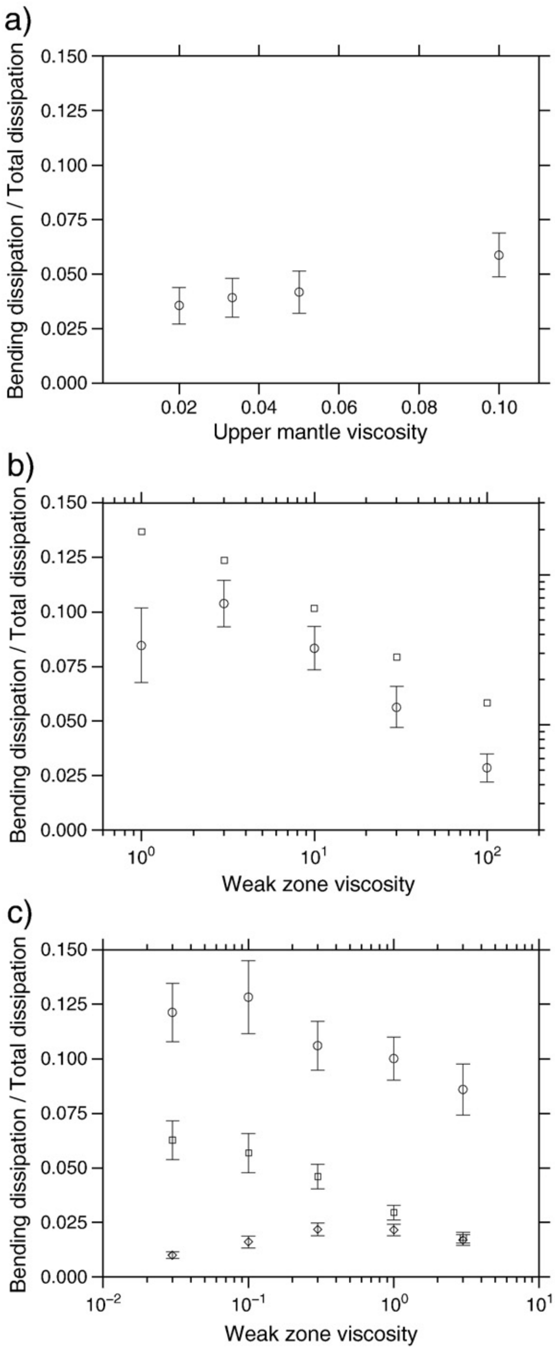

Fig. 8. (a) The ratios of the bending dissipation to the total dissipation versus upper mantle viscosity for cases with layered viscosity structure (cases C01–C04). (b) The ratios of the bending dissipation to the total dissipation versus weak zone viscosity (circles) for cases with both layered viscosity and weak zones (cases D01–D05, see Fig. 9 for the weak zone geometry). Squares show the non-dimensional surface velocity for these cases. (c) The ratios of the bending dissipation to the total dissipation versus weak zone viscosity (circles) for cases with curved weak zones (cases E01–E05, see Fig. 10a for the weak zone setup). Squares show ratios of the viscous dissipation in the curved bending slab region to the total dissipation. Diamonds show ratios of the viscous dissipation in the curved weak zones to the total dissipation.

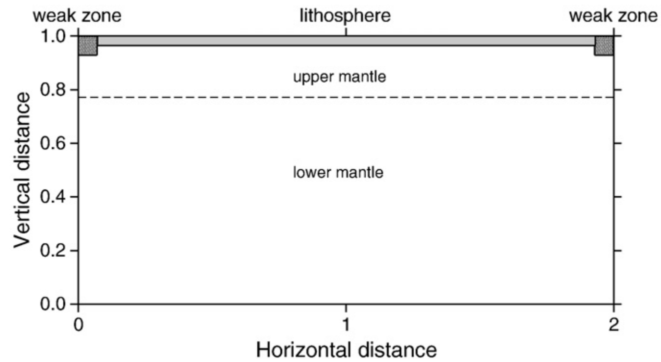

Fig. 9. The weak zone geometry for cases C01–C04. The shaded region shows the lithosphere and the dotted region shows the weak zones.

weak zone viscosity for cases D01–D05. When we gradually reduce the weak zone viscosity from 100.0 to 3.0 for cases D01–D04, Φ_b/Φ_{tot} gradually increases from 2.9% to 10.4% due to the increased surface velocity and subduction (Fig. 8b). However, further reducing the weaker zone viscosity to 1.0 (e.g. case D05) does not significantly affect Φ_b/Φ_{tot} any more (Fig. 8b). Fig. 2d, e and f show snapshots of temperature, viscous dissipation, and slab region and bending zones for case D03 after it reaches a statistically steady state.

It is worthwhile to further modify our weak zone setup to form a curved weak zone above the subducting slabs to better simulate the bending slabs. Starting from the case D03, we modify the weak zone setup at the upper-left corner (i.e. subduction zone, see Fig. 2d) but keep the weak zone at the upper-right corner unchanged. First, we significantly increase the numerical resolution to 10 km for this 200 km by 200 km zone through mesh refinement. The zone is then divided into four different regions by three circular arcs (Fig. 10a). Take the bottom-right corner as the center of a circle, and r as the distance to the center. The region with $r<100$ km is defined as the normal upper mantle region with reduced viscosity or $\eta_r(z)=1/30$; the region with 100 km$<r<$200 km is defined as the bending slab or lithospheric region with $\eta_r(z)=1$; the region with 200 km$<r<$240 km is the newly defined weak zone with a constant viscosity, η_{weak}, that represents the weak subduction zone fault; and the remaining region is defined as the overriding plate region with $\eta_r(z)=1$ (Fig. 10a). Through the weak zone setup in Fig. 10a, we obtain a bending slab region with a radius of curvature of 200 km.

We take the temperature field from the case D03 (Fig. 2d) as the initial condition and start a new case E03 with the weak zone setup discussed above. Case E03 is similar to the case D03, except that V_c is reduced to 10^4 and that the weak zone viscosity is reduced to 0.3 (Table 2). Fig. 10b shows a snapshot of viscosity and velocity distribution for case E03. It can be observed that the bending curvature is well simulated in our model. Fig. 10c and d show the corresponding viscous dissipation and detected bending zone in this 200 km by 200 km box. The Φ_b/Φ_{tot} is determined as 10.6% for case E03. However, it can be noticed that significant parts of viscous dissipation are generated in the weak zone outside of the bending slab region (Fig. 10c). Therefore the quantified bending dissipation of 10.6% should be taken as an upper bound. We also quantify the viscous dissipation generated in the bending slab region and the weak zone region as defined in Fig. 10a. The resulting viscous dissipation is 4.6% and 2.2% of the total viscous dissipation in these two regions, respectively (Fig. 8c). The sum of these two is smaller than Φ_b/Φ_{tot} (i.e. 10.6%) because the bending zone from our detection scheme includes region outside of the 200 km by 200 km box. The viscous dissipation in the weak zone (i.e. subduction zone fault) depends on the weak zone viscosity (Conrad and Hager, 1999a). We compute cases E01–E05 with weak zone viscosity varying from 3.0 to 0.03 (Table 2). The bending dissipation for these cases are similar, ~10% (Fig. 8c, Table 2). But the viscous dissipation in the weak zone decreases significantly compared with the viscous dissipation in the bending slab region (Fig. 8c). Notice that the detected bending zones from our detection scheme become quite small with smaller weak zone viscosity. Therefore we change the detecting parameter f_t from 0.5 to 0.3 for case E04 and E05 to ensure that the bending slab region

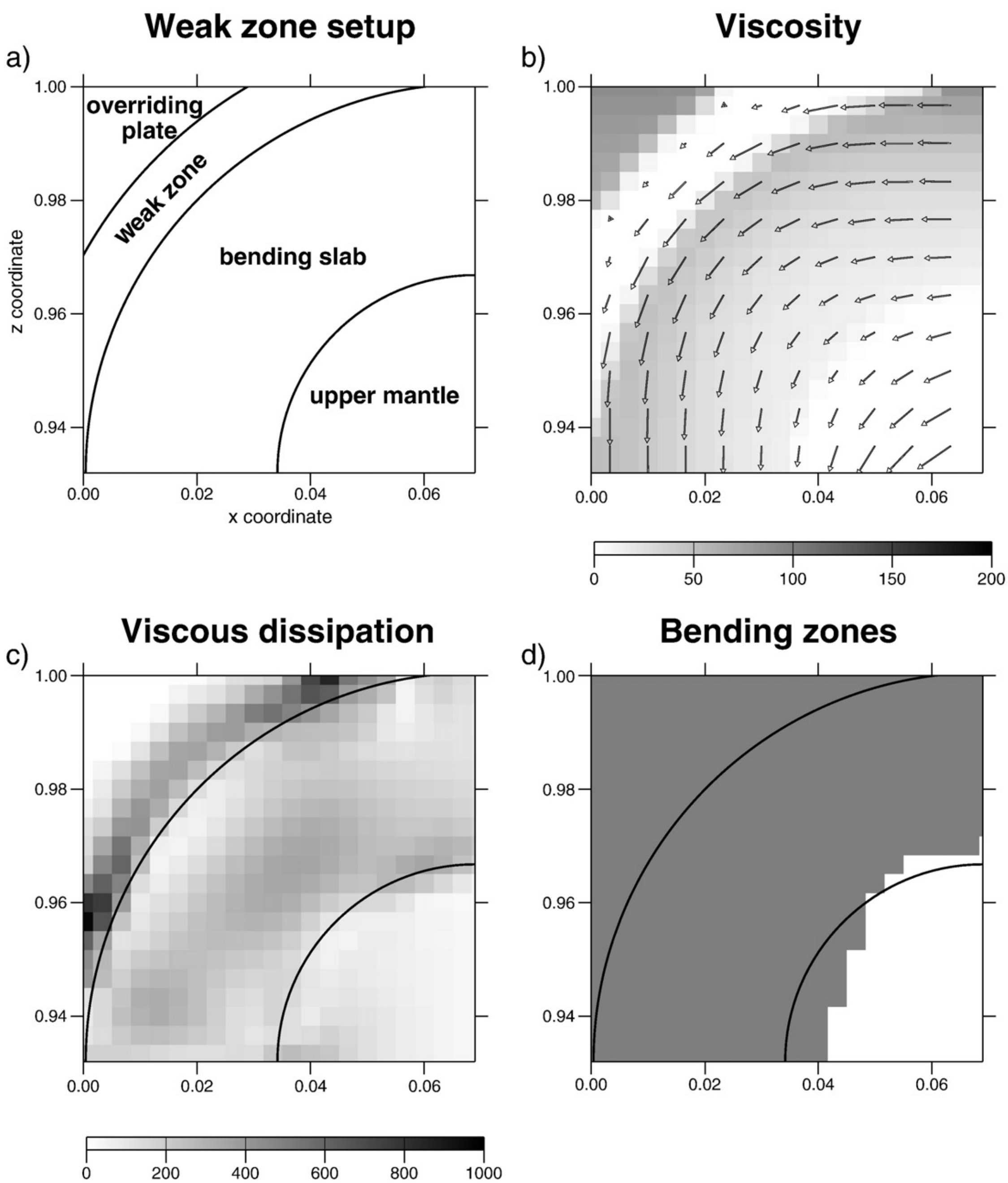

Fig. 10. (a) The geometry setup for the upper-left weak zone and curved subducted slab in case E01–E05. (b),(c) and (d) show a snapshot of viscosity, viscous dissipation and detected bending zones for case E03. All these values are non-dimensional. In (b), the arrows show the velocity field. In (c) and (d), the curved bending slab region is illustrated by the solid lines.

defined in Fig. 10a is completely included in the detected bending zones. As a result, we want to point out again that the Φ_b/Φ_{tot} we obtained here should be taken as an upper bound.

Although we only consider basal heating for all the cases discussed above, strong internal heating ratio, ~70%, is suggested for the Earth's mantle from the studies of mantle plumes (e.g., Davies, 1999; Zhong, 2006; Leng and Zhong, 2008b). Here we present cases with moderate internal heating ratio to show that Φ_b/Φ_{tot} are not sensitive to internal heating effects, although the ratio of total dissipation to surface heat flux is dependent on internal heating ratio (see Eq. (1)). Cases F01 and F02 are the same as case A01, except that we vary H in the energy Eq. (6) to add internal heating effect (Table 2). The internal heating ratio μ is computed as $\mu=(Q_s-Q_b)/Q_s$, where Q_s and Q_b are time-averaged surface heat flux and bottom heat flux after the model reaches a statistically steady state. For cases F01 and F02, μ is 19.9% and 42.0%, respectively. It can be observed that Φ_b/Φ_{tot} for cases F01 and F02 are similar to that for case A01, i.e. between 10% and 20% (Table 2). Similarly, cases F03 and F04 are the same as case D03, except that internal heating effects are included. μ is 18.9% and 35.5% for cases F03 and F04, respectively. Φ_b/Φ_{tot} for cases F03 and F04 are similar to that for case D03, i.e. less than 10% (Table 2). We also compute the ratios of the total dissipation to surface heat flux for these cases with internal heating and plot them in Fig. 6b. Note that although these cases all have $D_i=0.5$, according to Eq. (1), the ratio of the total dissipation to surface heat flux should be different due to their different internal heating ratio. Fig. 6b shows that Eq. (1) also works well for these internal heating cases.

4. Discussion

Buffett and Rowley (2006) estimated the bending dissipation for all the subduction zones as ~0.766 TW, and suggested that, if taking the Pacific plate as an example, the bending dissipation accounts for 40% of the gravitational potential energy released by slab buoyancy in the upper mantle. This bending dissipation would only account for 25% of the potential energy release for the upper mantle slabs, if all the major plates are considered (Buffett and Rowley, 2006). Conrad and Hager (1999a, 2001) concluded that 40% of the mantle's total dissipation happened in the plate bending zones. However, they only considered slabs penetrating to a shallow depth (~800 km) and ignored slab buoyancy flux in the deep mantle. The total dissipation in the Earth's mantle is equivalent to the total buoyancy flux of both sinking slabs and rising plumes in both upper mantle and lower mantle (Turcotte et al., 1974; Hewitt et al., 1975; Leng and Zhong, 2008a). Since the buoyancy flux structure in the Earth's mantle is not well constrained, it is difficult to estimate the total dissipation in the whole mantle. However, Eq. (3) enables us to estimate the total dissipation in compressible convection from the surface heat flux and dissipation number, both of which are known reasonably well. Considering the possible range of the total dissipation in the Earth's mantle that we estimated, 10.0–15.5 TW, the bending dissipation of 0.766 TW for present-day subduction zones estimated by Buffett and Rowley (2006) would only account for 5%–8% of the total dissipation. This relatively small ratio of bending dissipation to the total dissipation is consistent with our numerical results with more realistic viscosity structures including layered viscosity structure and weak plate margins (Table 2, Fig. 8).

From Eq. (3), the dissipation number controls the total dissipation in the Earth's mantle. In Eq. (2), given $\alpha_0 = 3\times10^{-5}$/K, $g_0 = 10$ m/s^2, $d = 2870$ km, and $C_{p_0} = 1200$ J/(kg K), the dissipation number is computed as 0.72. However, the thermal expansivity decreases with the pressure (or depth) and can be as small as 1×10^{-5}/K just above the core–mantle boundary (Chopelas and Boehler, 1989). Supposing that α decreases by a large factor of 5 from the surface to the core–mantle boundary, the averaged α is 1.8×10^{-5}/K, which corresponds to a dissipation number of 0.43. The range of dissipation number from 0.43 to 0.72 is consistent with the range explored in this study.

Due to the 2-D Cartesian geometry, the temperature variation across the bottom TBL is relatively small in our compressible mantle convection models and upwelling plumes are weak (e.g. Figs. 3a and 2a). Adding internal heating can further reduce the temperature contrast across the bottom TBL to unrealistically small values for the Earth's mantle. This is different from spherical models that produce larger temperature contrast in the bottom TBL for the same internal heating ratio (e.g. Leng and Zhong, 2008b). For our current study, we only consider a few cases with moderate internal heating ratio (Table 2). However, these cases have already shown that our results on the ratio of bending dissipation to total dissipation, Φ_b/Φ_{tot}, are not sensitive to the internal heating ratio. We therefore consider our results robust, even for cases with higher internal heating ratio.

Finally, for our compressible mantle convection cases with temperature-dependent viscosity (cases B01–B25 and case A01), we also use their surface heat flux (or Nusselt number) and Rayleigh number to fit the scaling law, $Q_s \sim Ra^{\beta}$, to determine the exponent β. For these cases with $D_i = 0.3$, 0.5 and 0.7, β is determined to be 0.3305, 0.2887 and 0.3201, respectively. This is similar to the results for incompressible convection (e.g. McKenzie et al., 1974), except that β is significantly smaller than 1/3 for cases with $D_i = 0.5$. We consider that this is caused by case B14, which has a smaller convection wavelength and surface velocity as we discussed before.

5. Conclusion

Our main conclusions can be summarized as following.

1) We provide an estimate for the total dissipation in the Earth's mantle as 10.0–15.5 TW based on the energetics of mantle convection (Hewitt et al., 1975) for reasonable ranges of mantle dissipation number (0.5–0.7) and internal heating ratio (~70%). The total dissipation is larger for smaller internal heating ratio.
2) Taking the bending dissipation for present-day subduction zones estimated by Buffett and Rowley (2006), we suggest that the bending dissipation only accounts for <10% of the total dissipation of Earth's mantle convection. Our estimated total dissipation and our conclusion on the relatively small fraction of bending dissipation in the total dissipation are independent of details of mantle convection such as mantle rheology and convection planform.
3) We quantified the relations between the total dissipation and the surface heat flux in 2-D Cartesian models of compressible mantle convection with strong temperature-dependent viscosity and different Rayleigh numbers and dissipation numbers. The results confirmed the relationship on the ratio of the total dissipation to surface heat flux derived by Hewitt et al. (1975).
4) We quantified the ratio of the bending dissipation to the total dissipation in our 2-D numerical models of compressible convection. The bending dissipation accounts for 10% to 20% of the total dissipation for the cases with only temperature-dependent viscosity. After including a weak upper mantle, the bending dissipation only accounts for less than 10% of the total dissipation. Adding weak zones at the plate margins and internal heating effects to the models does not significantly affect our results. These results from numerical models further support the conclusion that the bending dissipation only accounts for a small fraction (<10%) of the total dissipation from an independent method as outlined in conclusions 1 and 2. Collectively, our results are consistent with recent numerical, observational, and experimental studies on the bending dissipation (Wu et al., 2008; Capitanio et al., 2007, 2009; Krien and Fleitout, 2008; Schellart, 2009) and have important implications for thermal evolution models (Davies, 2009).

Acknowledgements

We thank Fabio Capitanio and Bruce Buffett for constructive reviews and Peter Molnar for insightful comments that helped to improve the manuscript. This study is supported by the National Science Foundation and David and Lucile Packard Foundation. The figures in this paper are plotted with GMT software <http://gmt.soest.hawaii.edu/>.

References

Balachandar, S., Yuen, D.A., Reuteler, D.M., Lauer, G.S., 1995. Viscous dissipation in three-dimensional convection with temperature-dependent viscosity. Science 267, 1150–1153.
Bercovici, D., Schubert, G., Glatzmaier, G.A., 1992. Three-dimensional convection of an infinite-Prandtl number compressible fluid in a basally heated spherical shell. J. Fluid Mech. 239, 683–719.
Birch, F., 1952. Elasticity and constitution of the Earth's interior. J. Geophys. Res. 57, 227–286.
Buffett, A.B., 2006. Plate force due to bending at subduction zones. J. Geophys. Res. 111, B09405, doi:10.1029/2006JB004295.
Buffett, A.B., Rowley, D.B., 2006. Plate bending at subduction zones: consequences for the direction of plate motions. Earth Planet Sci. Lett. 245, 359–364.
Capitanio, F.A., Morra, G., Goes, S., 2007. Dynamic models of downgoing plate-buoyancy driven subduction: subduction motions and energy dissipation. Earth Planet. Sci. Lett. 262, 284–297.
Capitanio, F.A., Morra, G., Goes, S., 2009. Dynamics of plate bending at the trench and slab-plate coupling. Geochem. Geophys. Geosyst. 10, Q04002. doi:10.1029/2008GC002348.

Chopelas, A., Boehler, R., 1989. Thermal expansion measurements at very high pressure, systematics, and a case for a chemically homogeneous mantle. Geophys. Res. Lett. 16, 1347–1350.
Conrad, C.P., Hager, B.H., 1999a. Effects of plate bending and fault strength at subduction zones on plate dynamics. J. Geophys. Res. 104 (17), 17551–17571.
Conrad, C.P., Hager, B.H., 1999b. The thermal evolution of an earth with strong subduction zones. Geophys. Res. Lett. 26, 3041–3044.
Conrad, C.P., Hager, B.H., 2001. Mantle convection with strong subduction zones. Geophys. J. Int. 144, 271–288.
Davies, G.F., 1993. Cooling the core and mantle by plume and plate flows. Geophys. J. Int. 115, 132–146.
Davies, G.F., 1999. Dynamic Earth: Plates, Plumes and Mantle Convection. Cambridge Univ. Press, New York. 458 pp.
Davies, G.F., 2009. Effect of plate bending on the Urey ratio and the thermal evolution of the mantle. Earth Planet. Sci. Lett. 287, 513–518.
Gurnis, M., 1989. A reassessment of the heat transport by variable viscosity convection with plates and lids. Geophys. Res. Lett. 16, 179–182.
Hager, B.H., Richards, M.A., 1989. Long-wavelength variations in Earth's geoid: physical models and dynamical implications. Phil. Trans. R. Soc. Lond. A 328, 309–327.
Hewitt, J.M., McKenzie, D.P., Weiss, N.O., 1975. Dissipative heating in convective flows. J. Fluid Mech. 68, 721–738.
Jarvis, G.T., McKenzie, D.P., 1980. Convection in a compressible fluid with infinite Prandtl number. J. Fluid Mech. 96, 515–583.
King, S.D., Lee, C.Y., van Keken, P.E., Leng, W., Zhong, S.J., Tan, E., Tosi, N., Kameyama, M.C., 2010. A community benchmark for 2D Cartesian compressible convection in the Earth's mantle, Geophys. J. Int. 180, 73–87.
Korenaga, J., 2006. Archean geodynamics and the thermal evolution of the Earth. In: Benn, K., Mareschal, J.-C., Condie, K.C. (Eds.), Archean Geodynamics and Environments, Geophysical monograph series 164, American Geophys. American Geophys. Union, Washington D.C., pp. 7–32.
Krien, Y., Fleitout, L., 2008. Gravity above subduction zones and forces controlling plate motions. J. Geophys. Res. 113, B09407. doi:10.1029/2007JB005270.
Leng, W., Zhong, S.J., 2008a. Viscous heating, adiabatic heating and energetic consistency in compressible mantle convection. Geophys. J. Int. 173, 693–702.
Leng, W., Zhong, S.J., 2008b. Controls on plume heat flux and plume excess temperature. J. Geophys. Res. 113, B04408. doi:10.1029/2007JB005155.
Leng, W., Zhong, S.J., 2009. More constraints on internal heating rate of the Earth's mantle from plume observations. Geophys. Res. Lett. 36, L02306. doi:10.1029/2008GL036449.
McKenzie, D.P., 1977. The initiation of trenches: a finite amplitude instability. In: Talwani, M., Pitman, W.C. (Eds.), Island Arcs, Deep Sea Trenches, and Back-Arc Basins, Maurice Ewing Series 1. Am. Geophys. Union, Washington, DC, pp. 57–61.
McKenzie, D.P., Jarvis, G., 1980. The conversion of heat into mechanical work by mantle convection. J. Geophys. Res. 85, 6093–6096.
McKenzie, D.P., Roberts, J.M., Weiss, N.O., 1974. Convection in the earth's mantle: towards a numerical simulation. J. Fluid Mech. 62, 465–538.
Moresi, L., Solomatov, V., 1995. Numerical investigation of 2D convection with extremely large viscosity variations. Phys. Fluids 7, 2154–2162.
Moresi, L., Zhong, S.J., Gurnis, M., 1996. The accuracy of finite element solutions of Stokes' flow with strongly varying viscosity. Phys. Earth Planet. Inter. 97, 83–94.
Pollack, H.N., Hurter, S.J., Johnson, J.R., 1993. Heat flow from the Earth's interior: analysis of the global data set. Rev. Geophys. 31, 267–280.
Schellart, W.P., 2009. Evolution of the slab bending radius and the bending dissipation in three-dimensional subduction models with a variable slab to upper mantle viscosity ratio. Earth Planet. Sci. Lett. 288, 309–319.
Turcotte, D.L., Schubert, G., 2002. Geodynamics, 2nd ed. Cambridge Univ. Press, New York.
Turcotte, D.L., Hsui, A.T., Torrance, K.E., Schubert, G., 1974. Influence of viscous dissipation on Benard convection. J. Fluid Mech. 64, 369–374.
Wu, B., Conrad, C.P., Heuret, A., Lithgow-Bertelloni, C., Lallemand, S., 2008. Reconciling strong slab pull and weak plate bending: the plate motion constraint on the strength of mantle slabs. Earth Planet Sci. Lett. 272, 412–421.
Zhong, S.J., 2006. Constraints on thermochemical convection of the mantle from plume heat flux, plume excess temperature and upper mantle temperature. J. Geophys. Res. 111, B04409. doi:10.1029/2005JB003972.